Graphitic-Based Solid-State Supercapacitors: Enabling Redox

Reaction by In-Situ Electrochemical Treatment

4   *Mojtaba Amjadipour[1], Dawei Su[2, 3], and Francesca Iacopi[1, 3*]*

5   [1]School of Electrical and Data Engineering, Faculty of Engineering and Information Technology,
6   University of Technology Sydney, NSW, Australia.

7   [2]School of Mathematical and Physical Sciences, Faculty of Science, University of Technology
8   Sydney, NSW, Australia.

9   [3]Centre for Clean Energy Technology, University of Technology Sydney, NSW, Australia.

12   **Abstract**

13   The quest for supercapacitors that can hold both high energy and power density is of increasing

14   significance as the need for green and reliable energy storage devices grows, for both large-scale

15   and integrated systems. While supercapacitors for integrated technologies require a solid-state

16   approach, gel-based electrolytes are generally not as efficient as their aqueous counterparts. Here

17   we demonstrate a strategy to enhance the performance of quasi-solid-state supercapacitors made

18   by graphitized silicon carbide on silicon electrodes and polyvinyl alcohol (PVA) + H_2SO_4 gel

19   electrolyte. The electrochemical characterization shows an increase of the specific capacitance of

20   the cell up to 3-fold resulting from a simple agent-free, in-situ, electrochemical treatment leading

21   to functionalization of the graphitic electrodes. The functionalization of the electrodes

simultaneously enables redox reactions, without adding any redox agent, and increases the double layer contribution to the overall capacitance. The strategy and insights offered by this work hold great promise for improving quasi-solid-state, miniaturized on-chip energy storage systems, which are compatible with silicon electronics.

1. Introduction

The rapid development of portable and wireless electronics has significantly increased the demand for integrated energy storage devices. Additionally, the emerging need for clean energy sources such as solar and wind energies further increases the demand for reliable and maintenance-free batteries and supercapacitors [1-2]. Electrochemical supercapacitors have attracted a lot of attention due to their high power density capability as storage devices [3-6]. Their environmentally friendly and long cyclability characteristics make electrochemical supercapacitors prominent candidates for future integrated energy storage devices [2, 7].

The charge storage in the electrochemical supercapacitors is based primarily on electrical double layer capacitance (EDLC), and to a smaller extent, on redox reactions or pseudocapacitance [1, 8]. EDLC relies on ions adsorption at the electrode/electrolyte interface in the presence of an electric field [9]. Redox reactions in supercapacitors store charge via a fast and reversible charge transfer reaction between electrolyte ions and the electrodes [10]. Those reactions are commonly introduced by adding a variety of external redox agents to the system and devising an appropriate functionalization of the electrodes [8, 11-15]. Some widely used redox additives to the electrolyte are P-phenylenediamine, hydroquinone and indigo carmine [16-17]. Overall, the amount, accessibility and quality of the interfaces between the electrode and electrolyte are critical to the performance of the supercapacitors.

Traditionally, supercapacitors are fabricated using liquid electrolytes, making them prone to undesirable electrolyte leakage issue [4, 18]. The packaging requirements needed to guarantee leakage-free cells makes them too large and unpractical for miniaturized applications. Therefore, gel-based electrolytes are an alternative solution to address this issue [3, 19-20]. The gel electrolytes can potentially also overcome other typical challenges of supercapacitors, such as corrosion, self-discharge, solvent evaporation, and consuming at elevated temperatures [4]. Gel electrolytes are often made of a mixture of a polymer (such as PVA) and an acid (typically H_2SO_4 or H_3PO_4) [1, 21]. PVA-acid based gel electrolytes have not been considered active redox materials. Therefore, the addition of redox agents has been the conventional way to enable the redox contribution in charge storage [11-13]. Moreover, gel electrolytes are generally not as efficient as their aqueous counterparts in terms of charge storage, among others, due to the low charge carrier mobilities [11, 22]. This fundamental limitation prompts the need for more research into mechanisms to enhance the performance of gel electrolytes.

Carbon-based materials such as graphite, graphene oxide, carbon nanotubes, and graphene have been widely explored as electrode materials for supercapacitors [1, 8, 23-26]. Graphene and graphitic carbon-based electrodes have proven to be a very promising choice due to their superior electrical and electrochemical properties, including high surface area and high conductivity [1]. While graphene-based electrodes are a preferred option for flexible devices [1, 23, 27], graphene or graphitic carbon directly fabricated on silicon substrates offer significant potential for on-chip supercapacitors that can be embedded in integrated circuits [8, 28-35]. Among various synthesis methods of graphene/graphitic carbon, a metal-based catalytic synthesis on silicon carbide on silicon stands out as one of the most versatile and compatible with the current semiconductor industry [30, 36-38]. It offers a binder-free approach to fabricate graphene with high adhesion and

1   tunable characteristics directly on silicon wafers [38]. Also, this approach can be employed for

2   miniaturization and wafer-level fabrication [30, 36-38].

3   In this work, we demonstrate the possibility of enhancing the performance of quasi-solid-state

4   supercapacitors on silicon using a $PVA+H_2SO_4$ gel electrolyte through an agent-free, in-situ

5   functionalization of graphitic carbon electrodes. We show that this procedure triggers redox

6   reactions not available with the as-prepared cells, in addition to improving the EDLC charge

7   storage contribution.

8   **2.   Results and Discussion**

9   The graphene synthesis on cubic silicon carbide using Ni metal catalyst layers, either alone or

10   alloyed with Cu, provides control over the defect density as well as the porosity of the

11   graphitized electrodes [36, 39]. We investigated and compared three different types of electrodes:

12   low-defect, oxidized and porous graphitic electrodes (refer to the Experimental Section).

13   Scanning electron microscopy (SEM) and atomic force microscopy (AFM) are used to compare

14   the surface morphology of the different electrode types. Both methods are in agreement,

15   revealing similar surface images. Open pores with dimensions of several microns are clearly

16   visible on the porous electrodes surface (**Figure 1c**, **S2c, 1f**). This porosity stems from a repeated

17   Ni diffusion, intrusion and removal of nickel silicides [39].

18   The oxidized (**Figure 1b**, **S2b, 1e**) and the low-defect electrodes (**Figure 1a**, **S2a, 1d**) do not

19   show significant porosity on the surface, but they reveal a finer granular pattern that seems to be

20   common across all of the electrode types. This pattern corresponds to particle sizes in the range

21   of 80-150 nm, which is also confirmed in the power spectral densities (PSD) extracted from the

22   AFM images. Although the PSDs for the different electrodes show very different distributions,

1   all of them show evident peaks at spatial frequencies in the 8-12 μm^{-1} range (**Figure S3**),

2   corresponding to the granularity discussed above. The RMS roughness estimated for the porous

3   electrodes is ~72 nm, which is significantly higher than the low-defect (~25 nm) and the

4   oxidized electrodes (~20 nm). The corresponding AFM height profiles in **Figures 1g, h** and **i**,

5   provide a further comparison of the different surface roughness.
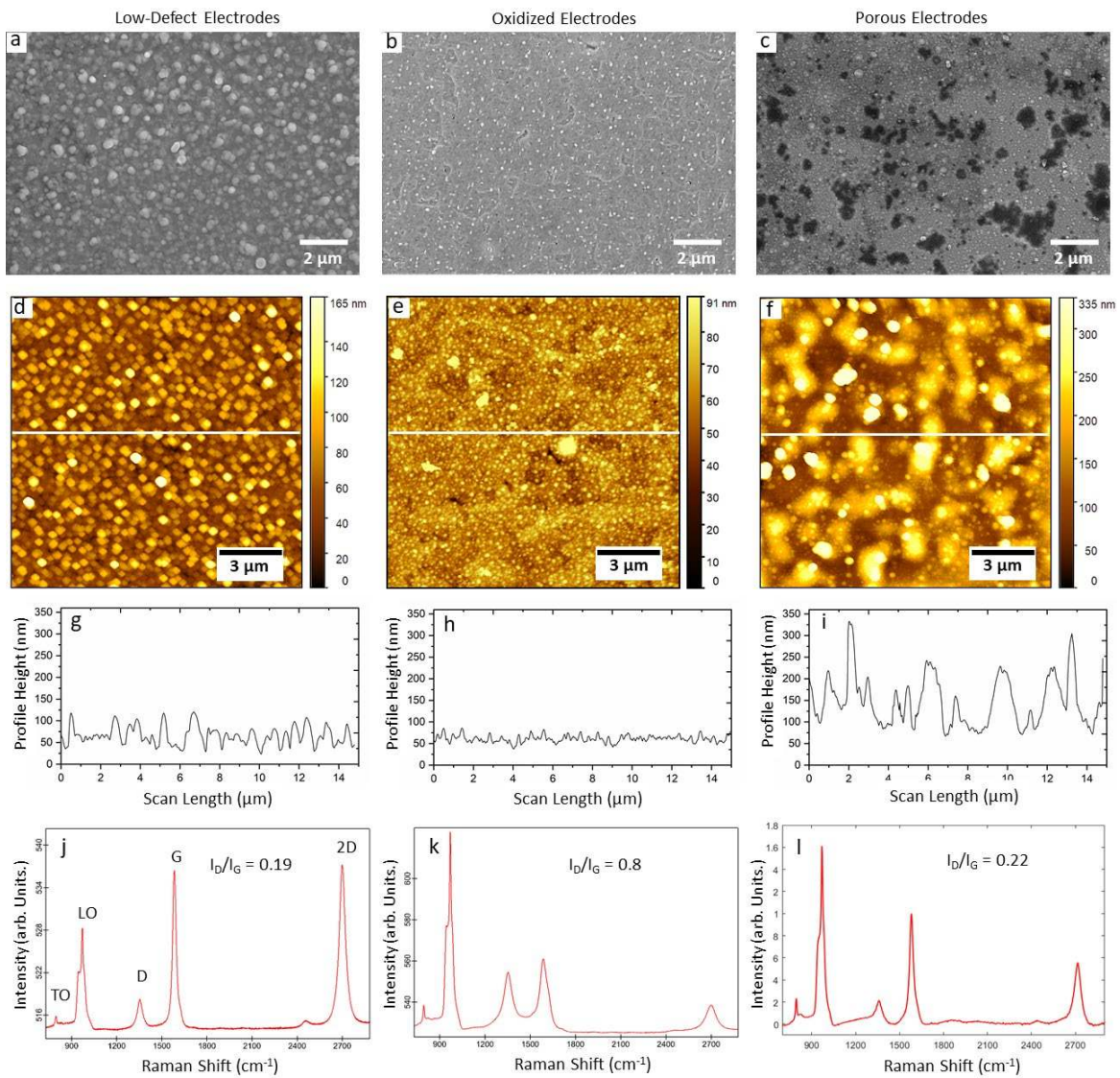
6

7   **Figure 1.** SEM images showing the surface morphology of the different graphitic electrodes: (a)

8   low-defect, fabricated via 10 nm Ni and 20 nm Cu catalytic layers; (b) oxidized, synthesized by

1   using a very thin Ni layer (~3 nm), and (c) porous, fabricated using two rounds of Ni graphitization.

2   AFM images of the (d) low-defect (e) oxidized, and (f) porous graphitic electrodes; the white

3   section lines represent where the height profiles are extracted. Height profiles for the (g) low-

4   defect (h), oxidized, and (i) porous graphitic electrodes. Raman spectra of (j) low-defect (k)

5   oxidized and (l) porous graphitic electrodes. These averaged spectra are collected over 2500 sites

6   over a 100 μm^2 area each.

7   Raman spectroscopy yields crucial information about the as-prepared graphitized electrodes.

8   Three distinct peaks in the Raman spectrum of graphitic carbon can be assigned to D, G, and 2D

9   bands, respectively [40-41]. The D band is activated by the presence of defects within the graphene

10   lattice, while G and 2D bands are related to the sp^2 bonded carbon lattice [41]. Among other

11   recognizable peaks in the Raman spectra (**Figure 1g-i**) are the TO (at ~850 cm^{-1}) and LO (at

12   ~972 cm^{-1}) silicon carbide peaks, which are related to the 3C-SiC/Si pseudo-substrate [42-43]. The

13   intensity ratio between D and G peaks (I_D/I_G) is commonly used as an indicator for graphene

14   defect density assessment, i.e. higher I_D/I_G ratios indicate a higher defect density [30]. As can be

15   noted from **Figure 1g-i**, the electrode graphitized by depositing Ni and Cu layers has the lowest

16   defect density (**Figure 1g**), while the sample fabricated by a 3 nm Ni layer has the highest defect

17   density (**Figure 1h**). These defects typically also translate into a high amount of oxidization in

18   the graphitic carbon due to a sensibly higher amount of chemically active sites (edges and

19   vacancy defects) available for bonding with oxygen species. The Raman spectra of the defective

20   graphitic electrodes match with previously reported spectra for oxidized graphene [44-45];

21   therefore, we refer to the highly defective graphitic electrodes as oxidized ones (**Figure 1h**).

22   **Figure 2** shows the cyclic voltammetry (CV) test results of the cells fabricated using the

23   electrodes in a sandwiched configuration (**Figure S1**). The initial CV curve represents a quasi-

1   rectangular shape which is the characteristics of EDLC-based charge storage (**Figure 2a**, **c,** and

2   **e**) [9]. No obvious indications of faradaic reactions are observed from the CV curves related to as-

3   prepared electrodes. The CV tests indicate that the cell fabricated with the oxidized electrodes

4   shows a significantly higher EDLC charge storage performance in the as-prepared condition

5   (larger area of the CV curve). This is expected, as the presence of oxygen species on the

6   graphitic surface offers more chemically active electrodes, which is desirable for an enhanced

7   EDLC [12].

8   Therefore, we have devised a strategy to enhance further the cell capacitance through an in-situ

9   electrochemical treatment of the electrodes. By charging the supercapacitor cells with potentials

10   beyond the water decomposition voltage (~1.2 V), we can expect to induce partial electrolysis of

11   the water content in the electrolyte. Charging the cells with 2V, would break water molecules

12   and generate chemically active and mobile species in the electrolyte, able to react in-situ with the

13   graphitic electrodes, particularly at their defective sites. Hence we explore this avenue as a

14   method to functionalize the electrodes electrochemically and in-situ, e.g. creating or enhancing

15   the amount of oxygen-containing functional groups on the electrodes' surface.

16   We show in **Figure 2** that this in-situ functionalization approach leads in fact to a significant

17   capacitance enhancement. The quasi-rectangular-area components of the CV curves show a

18   substantial increase after the functionalization process, indicating an EDLC enhancement.

19   Simultaneously, two faradaic peaks appear in the CV curves for all 3 types of cells, indicating

20   the triggering of redox reactions (**Figure 2b**, **d** and **f**). The total capacitance enhancement thus

21   results from a combination of an increase of the EDLC component as well as the enablement of

22   redox reactions in the cells. The redox peaks appear in two different regions: at 0.4 – 0.52 V

23   during the charging process and 0.09 – 0.2 V for the discharging process. It should be noted that

1   the redox peaks are here triggered without the addition of external redox agents [11, 18]. Aljafari et

2   al [18] have recently reported that the PVA+H$_2$SO$_4$ gel electrolyte can be a redox-active material.

3   However, they had not been able to observe evident faradaic peaks in their CV curves [18].
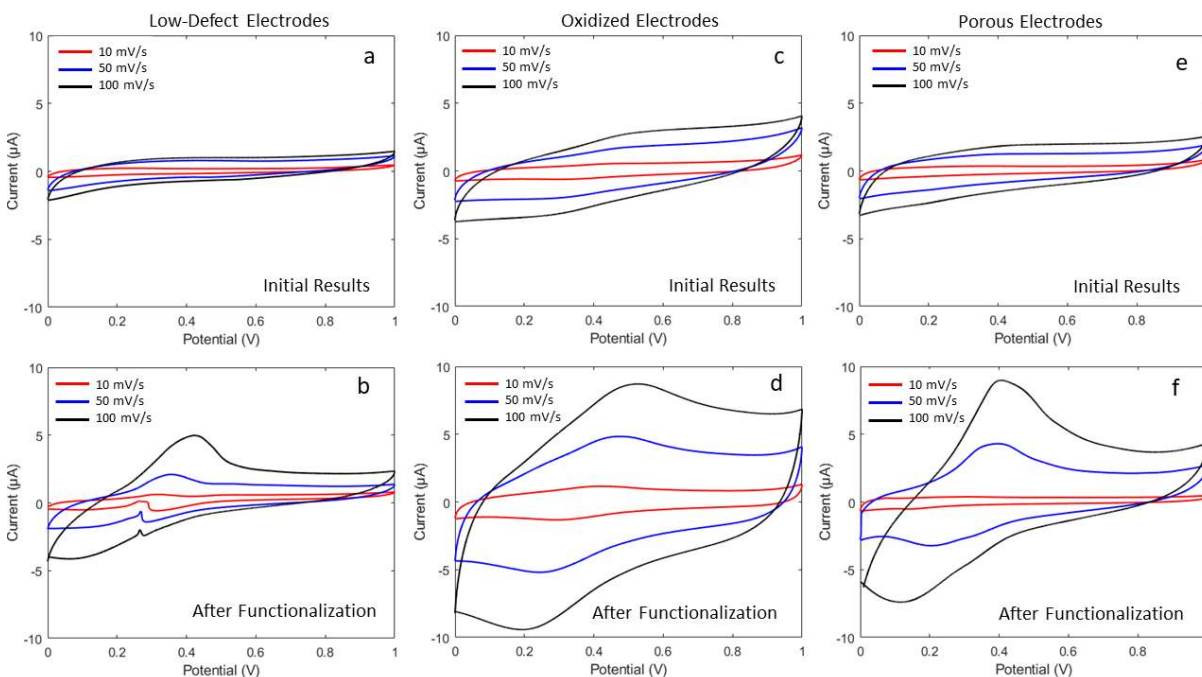
4

5   **Figure 2.** CV curves (a) initial results of cell fabricated by the low-defect graphitic electrodes; (b)

6   after functionalization; (c) initial results of the cell made of the oxidized electrodes; (d) after

7   functionalization; (e) initial results of cell fabricated by porous electrodes; (f) after

8   functionalization, where redox peaks are observed for all 3 types of electrodes/cells.

9   **Figure 3** shows the galvanostatic charge/discharge behavior of the cells. The charge/discharge

10   tests confirm that all cells fabricated with the oxidized electrodes show a significant enhancement

11   of charge storage after functionalization compared to their as-prepared counterparts. In particular,

12   the cell using oxidized electrodes shows an over 3-fold increase in capacitance after charging of

13   the cell at 2V for an in-situ functionalization (see values in **Table 1**). The fact that this type of cell

14   shows the largest extent of enhancement demonstrates that the initial density of chemically active

1   sites (or defects) is a key factor in the efficacy of the in-situ functionalization. In addition to the

2   capacitance enhancement, we observe a significant improvement also in the Coulombic efficiency,

3   particularly for the oxidized electrodes, as indicated by the data in **Table S1**.
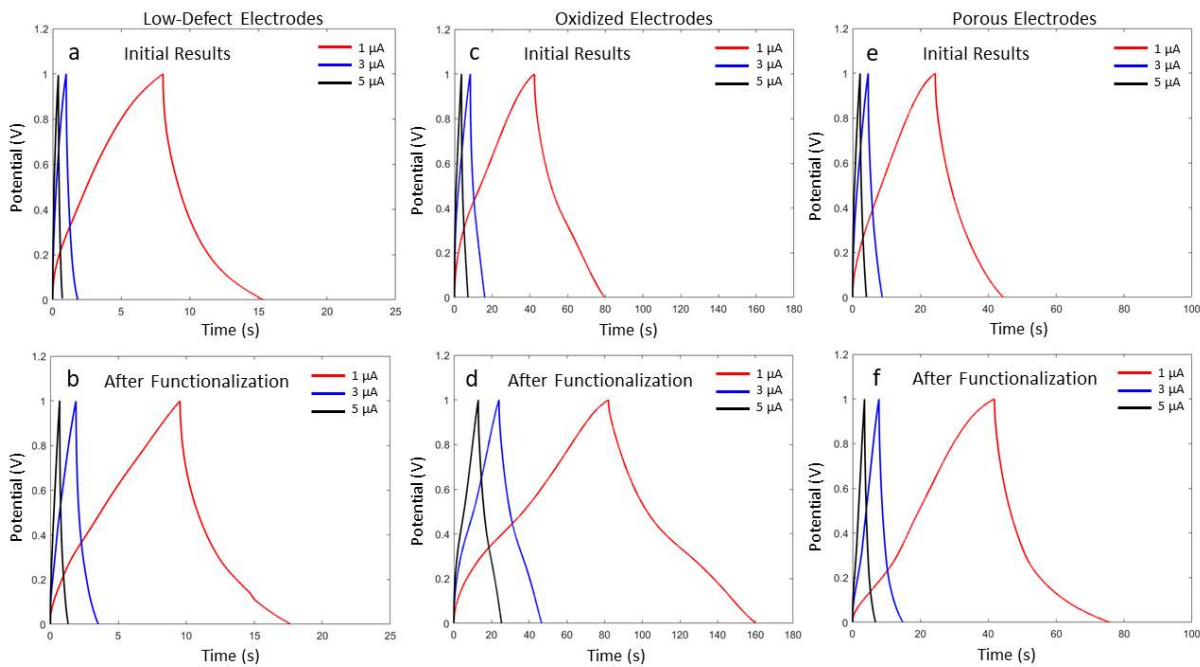
4

5   **Figure 3.** Galvanostatic charge/discharge (a) initial results of cell fabricated with the low-defect

6   graphitic electrodes (b) the same cell after functionalization (c) initial results of cell fabricated with

7   the oxidized electrodes (d) the same cell after functionalization (e) initial results of cell made of

8   the porous electrodes (f) the same cell after functionalization.

9

10

11   **Table 1.** Quasi-solid-state supercapacitors with different types of graphitic electrodes and their

12   performance calculated from galvanostatic charge/discharge tests. The electrodes' specific

13   capacitance before and after in-situ electrochemical functionalization are compared, showing a

14   substantial improvement after functionalization, particularly for the oxidized electrodes.

Electrode Type	I (μA)	C (μF/cm²)		
		Before functionalization	After functionalization	Improvement (%)
Oxidized	1	$110 \pm 1\%$	$255 \pm 1\%$	132
	3	$62 \pm 1\%$	$219 \pm 1\%$	253
	5	$43 \pm 1\%$	$195 \pm 1.5\%$	342
Porous	1	$54 \pm 1.5\%$	$70 \pm 2\%$	30
	3	$33 \pm 1\%$	$44 \pm 1\%$	32
	5	$24 \pm 1\%$	$35 \pm 1\%$	46
Low-defect	1	$16 \pm 1\%$	$19 \pm 1\%$	19
	3	$6 \pm 2\%$	$11 \pm 1\%$	83
	5	$4 \pm 2\%$	$7 \pm 1\%$	87

1

2 The electrochemical impedance spectroscopy was conducted before and after the functionalization

3 process. The Nyquist impedance plots for the cell fabricated with the oxidized electrodes show

4 that the cell resistance has slightly increased after the functionalization (**Figure 4a** and **b**). This

5 resistance increase is in agreement with the functionalization of the graphene electrodes [46].

6 Although the shapes of the curves are different, both other cell types show a similar increase in

7 transfer impedance after the in-situ functionalization process (**Figure S5**).
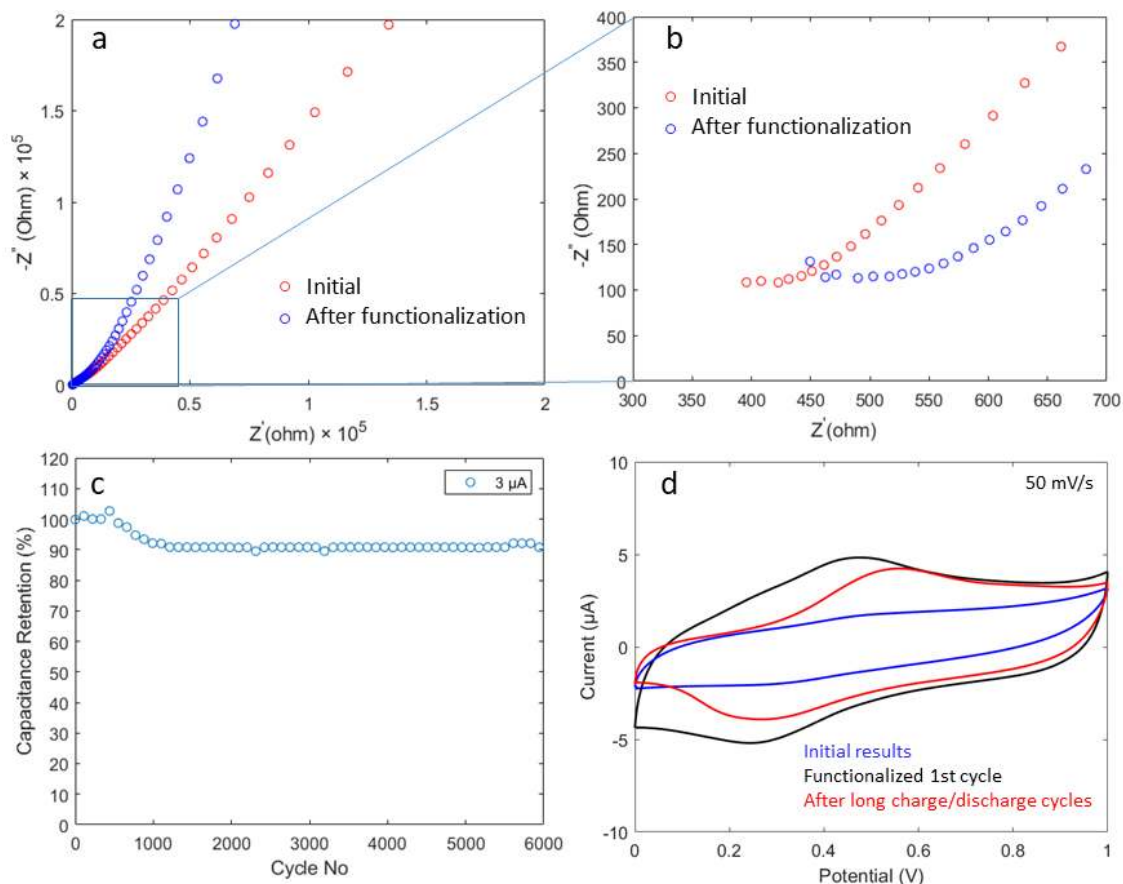
8 Long charge/discharge measurements of the cell fabricated with the oxidized graphitic electrodes

9 after the functionalization process show a reasonably long cyclability, with capacitance retention

10 of ~90% after 6000 cycles (**Figure 4c**). CV test results before and after the long charge/discharge

11 cycling tests still show the presence of the redox contribution, which appears thus to be a consistent

12 contribution to the overall cell capacitance after the functionalization (**Figure 4d**).

Figure 4. AC Impedance spectroscopy results of the cell fabricated with the oxidized electrodes (a) full spectra and (b) low impedance region. (c) Long cycling charge/discharge test results of the same cell (d) CV curves comparing the cell capacitance with as-prepared electrodes, after in-situ functionalization, and the latter after 6000 charge/discharge cycles, showing still substantially higher capacitance than the cell with as-prepared electrodes.

Figure 5a compares the Raman spectra of the oxidized electrodes before and after the functionalization process - the latter was collected by opening the cell after the in-situ functionalization, measuring through the electrolyte covering the graphitic electrode (inset in **Figure 5a**). While Raman spectroscopy does not show significant changes in the main graphitic peaks (D, G, and 2D), additional observed peaks at ~1435 cm^{-1} and ~2934 cm^{-1} stem from the PVA [47-48]. Joshi et al [47] reported similar spectra for graphene nanoribbons bonded to PVA.

11

1   The FTIR spectrum of the as-prepared oxidized electrodes in **Figure 5b** shows peaks related to

2   the 3C-SiC, TO peak at 794 cm^{-1}, LO at 970 cm^{-1}, in addition to a peak around 1060 cm^{-1} which

3   is commonly attributed to the epoxy functional groups and a peak at ~1225 cm^{-1} which originates

4   from the hydroxyl functional groups [49-52]. FTIR spectra of the oxidized electrodes after the in-

5   situ electrochemical treatment confirm the enhanced presence of oxygen functional groups on the

6   surface (**Figure 5b and S7**). A significant intensity increase of the peak around 1060 cm^{-1} after

7   the functionalization process of about 30% supports the enhancement of the oxygen functional

8   groups at the graphitic electrodes' surface. Energy-dispersive X-ray spectroscopy (EDS)

9   measurements also show a sixfold increase in the overall amount of oxygen species after
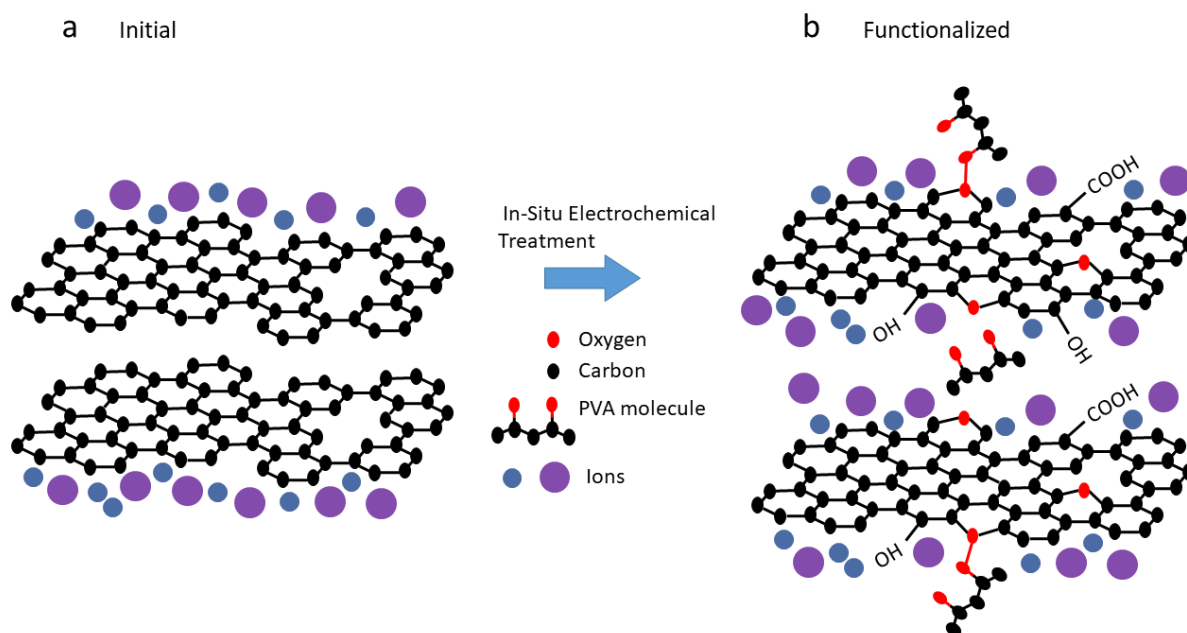
10   functionalization (**Figure S6**).

11   In light of all of the information above, we propose a likely mechanism for the enhanced

12   supercapacitor performance. We suggest that charging the supercapacitors with potentials over

13   the water decomposition voltage splits some of the water molecules within the electrolyte,

14   creating free hydroxyl groups, which can then react with the graphitic electrodes' surface

15   forming oxygen-containing groups, including epoxy. The possibility of such surface chemical

16   reactions has been previously supported in the literature [53-54]. Using first-principles calculations,

17   Ghaderi and Peressi [53] have indicated that hydroxyl ions can convert and form epoxy groups on

18   the graphene surface. This mechanism leads to a simple, in-situ preparation of functionalized

19   electrodes, which is the key to triggering redox reactions and enhancing the EDLC performance.
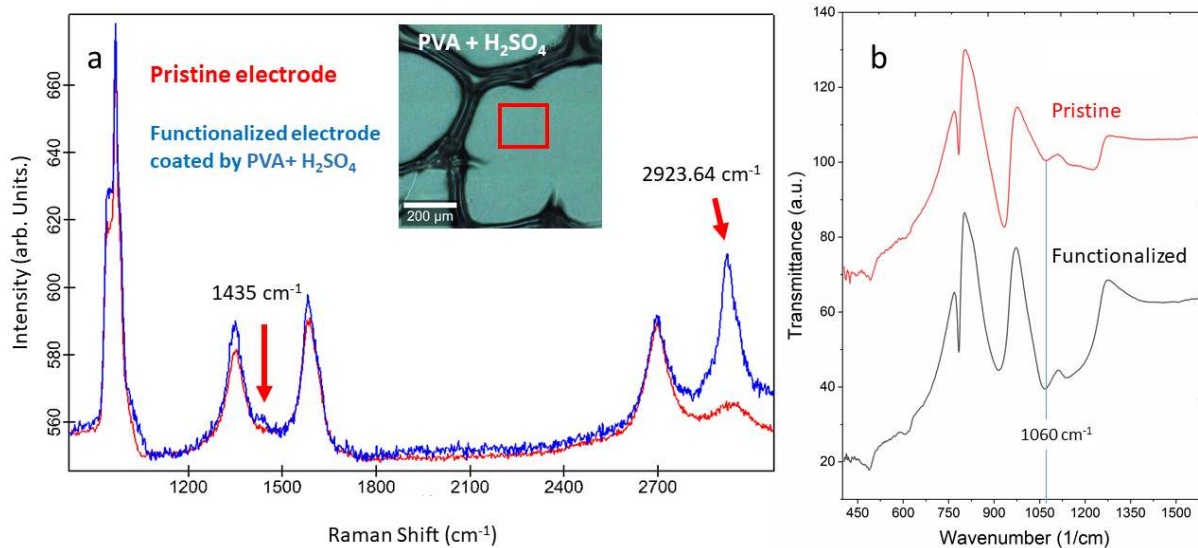
Figure 5. (a) Raman spectra of the oxidized electrodes, inset shows an optical image of the area measured by Raman, and (b) FTIR spectra, before and after the agent-free in-situ functionalization of the oxidized electrodes (electrolyte removed).

In addition, the elevated amount of oxygen functional groups induced on the graphitic surface by the functionalization process is expected to significantly increase the graphene inter-layer spacing, potentially up to ~0.45 nm as we have recently shown [49]. An increased inter-layer spacing, as well as an anticipated improved wettability of the graphitic electrodes due to the functionalization, would enable the PVA molecules to diffuse more efficiently between the electrode layers and intercalate the graphene, overall greatly enhancing the total extent of electrode/electrolyte interface in the cell, hence the EDLC capacitance (see schematic in **Figure 6**). Note that the PVA does not necessarily need to become chemically bonded to the graphitic electrodes for this mechanism to take place. We also note that the Coulombic efficiency improvement is likely a result of the enhanced electrode/electrolyte intercalation, leading likely to shorter ionic transport paths.

These data also show the importance of chemically-active graphitic electrodes in triggering redox reactions using a PVA+H₂SO₄ gel electrolyte [22]. We suggest that the redox reaction at the electrode/electrolyte interface originates from the elevated presence of oxygen functional groups [55]. Although we do not exclude the possibility for additional surface mechanisms, we believe that the most likely redox reaction is the repetitive transformation of the hydroxyl groups to the epoxy groups at the interface ($hydroxyl \leftrightarrow epoxy + 2H^+ + 2e^-$). Also, some redox contribution may arise from the reaction suggested by Aljafari et al [18] through reacting part of the OH branches in the PVA with the H₂SO₄ anions within the volume of the gel electrolyte.

Figure 6. A schematic representation of the agent-free in-situ functionalization mechanism leading to a significant capacitance improvement; (a) as-prepared electrodes (b) electrodes after the functionalization.

14

3. Conclusions

In summary, we have demonstrated a methodology to enable stable redox reactions in PVA-H_2SO_4 gel electrolytes without the addition of external redox agents. This method relies on generating oxygen functional groups by inducing hydrolysis of water molecules within the gel electrolyte, which promotes functionalization of the graphitic electrodes, particularly at the defective sites of the as-prepared electrodes. This leads to the performance enhancement of quasi-solid-state supercapacitors made of graphitic electrodes and PVA+H_2SO_4 gel electrolyte. The redox reactions at the electrode/electrolyte interface arise from the elevated presence of oxygen functional groups on the electrode's surface. Also, we show that the oxygen functionalization simultaneously improves the double-layer contribution to the overall capacitance thanks to improved electrolyte intercalation of the graphitic electrodes. The functionalized cells exhibit a promising electrochemical performance with good cycling stability.

These insights indicate a simple path to significantly enhance the performance of supercapacitors using gel-based electrolytes, which are key to the fabrication of quasi-solid-state supercapacitors. This approach offers a new path to develop further miniaturized on-chip energy storage systems, which are compatible with silicon electronics and can support the power demand to operate integrated smart systems.

4. Experimental Section

4.1 Preparation of the electrodes

3C-SiC (cubic polytype) films, epitaxially grown on Si (100) substrates have been purchased from NOVASiC. The silicon carbide layers are ~500 nm thick and have been chemically and mechanically polished (StepSiC® by NOVASIC (France)) [56]. The graphitization of the SiC

1 films has been carried out using a solid-source approach mediated by a catalytic metal alloy [36-

2 37]. The metal layers, either only a Ni or a combination of Ni and Cu, were sputtered on the 3C-

3 SiC/Si(100) substrates using a Cryopump deposition chamber with CD Ar^+ ion and 200 mA

4 current. The sputtering rates for Ni and Cu were ~ 0.05 nm/s and ~ 0.1 nm/s, respectively. The

5 metal-coated substrates were annealed to ~1100 °C (25 °C /min) for an hour under vacuum

6 condition (~10^{-5} mbar). The high-temperature annealing in the presence of the metallic layer

7 promotes the breakage of Si-C bonds on the SiC surface to form Ni silicides. The released

8 atomic C is then available to form graphene or graphitic carbon, depending on the selected

9 catalytic layer and process. The remaining metal residues and reaction by-products were

10 removed using a chemical wet etching for ~ 9 h (Freckle solution, for detailed information on

11 this approach, refer to [36-37]).

12 Low-defect graphitic electrodes were synthesized by depositing a Ni layer (~10 nm) and a Cu

13 layer (~ 20 nm) over the SiC surface, followed by an annealing process at 1100°C (**Figure 1a**

14 and **g**). The use of a single thin Ni catalyst layer (~ 3 nm) leads to substantially more defective

15 and oxidized graphene (**Figure 1h**). As the Ni layer is very thin, a significant amount of the

16 catalyst film is transformed into nickel oxide upon exposure to air [57-58], leading to the synthesis

17 of graphene with a high content of oxygen (oxidized electrodes). The electrodes were left

18 intentionally exposed to air for at least 24 hours before the high-temperature annealing to

19 promote the oxidation of nickel. Kenney et al. [58] report that the native nickel oxide thickness is

20 limited to ~ 2 nm. Finally, in order to prepare a porous graphitic electrode, the single catalyst

21 (Ni) procedure were repeated for a few cycles [39]. Here, we have employed two cycles of Ni

22 deposition (~ 8 nm), annealing and Freckle wet etching, leading to a rough surface with open

23 porosity (**Figure 1c** and **f**).

4.2 Fabrication of the quasi-solid-state supercapacitors

Quasi-solid-state supercapacitors were fabricated using a sandwich cell design (**Figure S1**). This design is based on using two electrodes ($\sim 2 \times 1$ cm^2) with a gel electrolyte in between the electrodes (the working area is ~ 0.9 cm^2) [19]. The cells were sealed with Kapton tape and stored for a few hours before testing. The typical thickness of the gel electrolyte used here is ~ 300 μm. The PVA+H$_2$SO$_4$ gel electrolyte was prepared by adding 3g PVA molecule (99 % purity and 108K molecular weight) to 30 mL deionized (DI) water followed by the addition of 3g of H$_2$SO$_4$ (98%) and stirring at 80 °C for a few hours to become completely transparent.

4.3 Characterization

The electrode surface was imaged using a Zeiss Supra 55VP scanning electron microscope (SEM) operating at 10 KeV and Dimension 3100 SPM atomic force microscope (AFM) by non-contact mode. The samples were cleaned using acetone, isopropanol, and de-ionized water before SEM and AFM measurements and were mounted on the sample holders using double-sided copper tape. SEM and AFM characterizations were conducted on the same electrodes used to fabricate the devices. EDS measurement was conducted using a Zeiss Supra 55VP SEM (10 KeV). Raman spectra were measured using a WiTec Raman microscope equipped with a green wavelength (532 nm) laser, by collecting maps over 100 μm^2 areas, made of 2500 single spectra. The Raman data reported is the average of the collected spectra from such maps. The FTIR measurements were conducted at room temperature using a Thermo Scientific Nicolet 6700 ATR-FTIR for the entire wavelength range (400 - 4000 cm^{-1}). The data was collected 64 times and the data reported here is the average spectra. The peak intensity was calculated based on the peak area. The FTIR data reported for the functionalized sample is collected on the cleaned

1 electrode after opening the cell. The electrodes were cleaned by sonication in de-ionized water

2 until no electrolyte residue was observable.

3 **4.4 Electrochemical characterization**

4 The electrochemical performance of the supercapacitors was evaluated with an electrochemical

5 workstation (CH Instruments, 660 E Model) in a two-probe configuration (**Figure S1 b**).

6 Galvanostatic charge/discharge (CD) measurements were performed at room temperature with

7 different currents: 1-5 µA with a potential window of 1 V. Data reported here are the averaged

8 values calculated from 5 to 10 charge/discharge cycles. The CD test was used for assessing the

9 supercapacitor's stability over 6000 cycles using 3 µA current and 1 V potential window. The

10 areal specific capacitance of the electrodes (C) was calculated based on the CD data using

11 equation 1 over the discharge period of the curve [14, 59]

$$ 12 \qquad C = 4I \times \frac{2 \int V dt}{V^2 |_{V_i}^{V_f}} \qquad (1) $$

13 where C is the areal specific capacitance of the electrodes in ($\mu F cm^{-2}$), I represent the current

14 density ($\mu A cm^{-2}$), V is the CD potential (V), V_i and V_f are the initial and final voltages in the

15 discharge cycle (V). $\int V dt$ represents the area under the CD discharge curve. The Coulombic

16 efficiency of the supercapacitors was estimated by $100 \times \int V dt|_d / \int V dt|_c$, where d and c

17 represent the discharge and charge periods.

18 Electrochemical Impedance Spectroscopy measurements were performed in a 0.01 Hz to 100

19 KHz frequency range with a signal amplitude of 5 mV.

1   The in-situ functionalization process was performed at room temperature by charging the cells

2   with 1 or 3 µA current for ~10 minutes in a 2V potential window.

3

4   **Corresponding Author**

5   ***E-mail:** <ins>francesca.iacopi@uts.edu.au</ins>

6   **Author Contributions**

7   The manuscript was written through the contributions of all authors. All authors have given

8   approval to the final version of the manuscript.

17   **References**

18   [1]   J. Liang; A. K. Mondal; D.-W. Wang; F. Iacopi, Graphene-based planar
19   microsupercapacitors: recent advances and future challenges. *Advanced Materials Technologies*
20   **2019,** *4* (1), 1800200.
21   [2]   C. Liu; F. Li; L. P. Ma; H. M. Cheng, Advanced materials for energy storage. *Advanced*
22   *Materials* **2010,** *22* (8), E28-E62.
23   [3]   Z. Niu; L. Zhang; L. Liu; B. Zhu; H. Dong; X. Chen, All‑solid‑state flexible ultrathin
24   micro‑supercapacitors based on graphene. *Advanced Materials* **2013,** *25* (29), 4035-4042.

[4]   C.-H. Chang; B. Hsia; J. P. Alper; S. Wang; L. E. Luna; C. Carraro; S.-Y. Lu; R. Maboudian, High-temperature all solid-state microsupercapacitors based on SiC nanowire electrode and YSZ electrolyte. *ACS applied materials & interfaces* **2015,** *7* (48), 26658-26665.

[5]   J. Li; S. Sollami Delekta; P. Zhang; S. Yang; M. R. Lohe; X. Zhuang; X. Feng; M. Östling, Scalable fabrication and integration of graphene microsupercapacitors through full inkjet printing. *ACS Nano* **2017,** *11* (8), 8249-8256.

[6]   W. Hooch Antink; Y. Choi; K. d. Seong; J. M. Kim; Y. Piao, Recent progress in porous graphene and reduced graphene oxide‐based nanomaterials for electrochemical energy storage devices. *Advanced Materials Interfaces* **2018,** *5* (5), 1701212.

[7]   E. Frackowiak; F. Beguin, Carbon materials for the electrochemical storage of energy in capacitors. *Carbon* **2001,** *39* (6), 937-950.

[8]   M. Conte, Supercapacitors technical requirements for new applications. *Fuel Cells* **2010,** *10* (5), 806-818.

[9]   J. R. Miller; R. Outlaw; B. Holloway, Graphene double-layer capacitor with ac line-filtering performance. *Science* **2010,** *329* (5999), 1637-1639.

[10]   M. Toupin; T. Brousse; D. Bélanger, Charge storage mechanism of MnO2 electrode used in aqueous electrochemical capacitor. *Chemistry of Materials* **2004,** *16* (16), 3184-3190.

[11]   G. Ma; M. Dong; K. Sun; E. Feng; H. Peng; Z. Lei, A redox mediator doped gel polymer as an electrolyte and separator for a high performance solid state supercapacitor. *Journal of Materials Chemistry A* **2015,** *3* (7), 4035-4041.

[12]   Y. Xu; Z. Lin; X. Huang; Y. Wang; Y. Huang; X. Duan, Functionalized graphene hydrogel‐based high‐performance supercapacitors. *Advanced Materials* **2013,** *25* (40), 5779-5784.

[13]   Y. Fang; B. Luo; Y. Jia; X. Li; B. Wang; Q. Song; F. Kang; L. Zhi, Renewing functionalized graphene as electrodes for high‐performance supercapacitors. *Advanced Materials* **2012,** *24* (47), 6348-6355.

[14]   L.-Q. Fan; Q.-M. Tu; C.-L. Geng; J.-L. Huang; Y. Gu; J.-M. Lin; Y.-F. Huang; J.-H. Wu, High energy density and low self-discharge of a quasi-solid-state supercapacitor with carbon nanotubes incorporated redox-active ionic liquid-based gel polymer electrolyte. *Electrochimica Acta* **2020,** *331*, 135425.

[15]   L. Wang; Z. Sofer; M. Pumera, Will any crap we put into graphene increase its electrocatalytic effect? *ACS Nano* **2020**.

[16]   H. Yu; J. Wu; L. Fan; K. Xu; X. Zhong; Y. Lin; J. Lin, Improvement of the performance for quasi-solid-state supercapacitor by using PVA–KOH–KI polymer gel electrolyte. *Electrochimica Acta* **2011,** *56* (20), 6881-6886.

[17]   H. Yu; J. Wu; L. Fan; Y. Lin; K. Xu; Z. Tang; C. Cheng; S. Tang; J. Lin; M. Huang, A novel redox-mediated gel polymer electrolyte for high-performance supercapacitor. *Journal of Power Sources* **2012,** *198*, 402-407.

[18]   B. Aljafari; T. Alamro; M. K. Ram; A. Takshi, Polyvinyl alcohol-acid redox active gel electrolytes for electrical double-layer capacitor devices. *Journal of Solid State Electrochemistry* **2018**, 1-9.

[19]   B. Wang; M. Ahmed; B. Wood; F. Iacopi, All-solid-state supercapacitors on silicon using graphene from silicon carbide. *Applied Physics Letters* **2016,** *108* (18), 183903.

[20]   Y. Xu; Z. Lin; X. Huang; Y. Liu; Y. Huang; X. Duan, Flexible solid-state supercapacitors based on three-dimensional graphene hydrogel films. *ACS Nano* **2013,** *7* (5), 4042-4049.

[21]   B. Karaman; A. Bozkurt, Enhanced performance of supercapacitor based on boric acid doped PVA-H2SO4 gel polymer electrolyte system. *International Journal of Hydrogen Energy* **2018,** *43* (12), 6229-6237.

[22]   C. Zhong; Y. Deng; W. Hu; J. Qiao; L. Zhang; J. Zhang, A review of electrolyte materials and compositions for electrochemical supercapacitors. *Chemical Society Reviews* **2015,** *44* (21), 7484-7539.

[23]   Y. Zhao; J. Liu; B. Wang; J. Sha; Y. Li; D. Zheng; M. Amjadipour; J. MacLeod; N. Motta, Supercapacitor electrodes with remarkable specific capacitance converted from hybrid graphene Oxide/NaCl/Urea Films. *ACS Applied Materials & Interfaces* **2017,** *9* (27), 22588-22596.

[24]   M. S. Kim; B. Hsia; C. Carraro; R. Maboudian, Flexible micro-supercapacitors with high energy density from simple transfer of photoresist-derived porous carbon electrodes. *Carbon* **2014,** *74*, 163-169.

[25]   Y. Liang; W. Zhang; D. Wu; Q. Q. Ni; M. Q. Zhang, Interface Engineering of Carbon‐Based Nanocomposites for Advanced Electrochemical Energy Storage. *Advanced Materials Interfaces* **2018,** *5* (14), 1800430.

[26]   L.-Q. Fan; G.-J. Liu; C.-Y. Zhang; J.-H. Wu; Y.-L. Wei, Facile one-step hydrothermal preparation of molybdenum disulfide/carbon composite for use in supercapacitor. *International Journal of Hydrogen Energy* **2015,** *40* (32), 10150-10157.

[27]   B. Wang; J. Liu; Y. Zhao; Y. Li; W. Xian; M. Amjadipour; J. MacLeod; N. Motta, Role of graphene oxide liquid crystals in hydrothermal reduction and supercapacitor performance. *ACS Applied Materials & Interfaces* **2016,** *8* (34), 22316-22323.

[28]   A. Ouerghi; M. Marangolo; R. Belkhou; S. El Moussaoui; M. Silly; M. Eddrief; L. Largeau; M. Portail; B. Fain; F. Sirotti, Epitaxial graphene on 3C-SiC (111) pseudosubstrate: Structural and electronic properties. *Physical Review B* **2010,** *82* (12), 125445.

[29]   M. Amjadipour; A. Tadich; J. J. Boeckl; J. Lipton-Duffin; J. MacLeod; F. Iacopi; N. Motta, Quasi free-standing epitaxial graphene fabrication on 3C–SiC/Si(111). *Nanotechnology* **2018,** *29* (14), 145601.

[30]   N. Mishra; J. Boeckl; N. Motta; F. Iacopi, Graphene growth on silicon carbide: a review. *Physica Status Solidi (a)* **2016,** *213* (9), 2277-2289.

[31]   C. Riedl; C. Coletti; U. Starke, Structural and electronic properties of epitaxial graphene on SiC (0 0 0 1): a review of growth, characterization, transfer doping and hydrogen intercalation. *Journal of Physics D: Applied Physics* **2010,** *43* (37), 374009.

[32]   W. A. De Heer; C. Berger; M. Ruan; M. Sprinkle; X. Li; Y. Hu; B. Zhang; J. Hankinson; E. Conrad, Large area and structured epitaxial graphene produced by confinement controlled sublimation of silicon carbide. *Proceedings of the National Academy of Sciences* **2011,** *108* (41), 16900-16905.

[33]   S. Wang; B. Hsia; C. Carraro; R. Maboudian, High-performance all solid-state micro-supercapacitor based on patterned photoresist-derived porous carbon electrodes and an ionogel electrolyte. *Journal of Materials Chemistry A* **2014,** *2* (21), 7997-8002.

[34]   F. Liu; A. Gutes; I. Laboriante; C. Carraro; R. Maboudian, Graphitization of n-type polycrystalline silicon carbide for on-chip supercapacitor application. *Applied Physics Letters* **2011,** *99* (11), 112104.

[35]   B. Hsia; M. S. Kim; M. Vincent; C. Carraro; R. Maboudian, Photoresist-derived porous carbon for on-chip micro-supercapacitors. *Carbon* **2013,** *57*, 395-400.

[36]   F. Iacopi; N. Mishra; B. V. Cunning; D. Goding; S. Dimitrijev; R. Brock; R. H. Dauskardt; B. Wood; J. Boeckl, A catalytic alloy approach for graphene on epitaxial SiC on silicon wafers. *Journal of Materials Research* **2015,** *30* (05), 609-616.

[37]   N. Mishra; J. J. Boeckl; A. Tadich; R. T. Jones; P. J. Pigram; M. Edmonds; M. S. Fuhrer; B. M. Nichols; F. Iacopi, Solid source growth of graphene with Ni–Cu catalysts: towards high quality in situ graphene on silicon. *Journal of Physics D: Applied Physics* **2017,** *50* (9), 095302.

[38]   B. V. Cunning; M. Ahmed; N. Mishra; A. R. Kermany; B. Wood; F. Iacopi, Graphitized silicon carbide microbeams: wafer-level, self-aligned graphene on silicon wafers. *Nanotechnology* **2014,** *25* (32), 325301.

[39]   M. Ahmed; B. Wang; B. Gupta; J. J. Boeckl; N. Motta; F. Iacopi, On-silicon supercapacitors with enhanced storage performance. *Journal of The Electrochemical Society* **2017,** *164* (4), A638-A644.

[40]   L. Malard; M. Pimenta; G. Dresselhaus; M. Dresselhaus, Raman spectroscopy in graphene. *Physics Reports* **2009,** *473* (5), 51-87.

[41]   A. C. Ferrari, Raman spectroscopy of graphene and graphite: disorder, electron–phonon coupling, doping and nonadiabatic effects. *Solid State Communications* **2007,** *143* (1), 47-57.

[42]   F. Iacopi; G. Walker; L. Wang; L. Malesys; S. Ma; B. V. Cunning; A. Iacopi, Orientation-dependent stress relaxation in hetero-epitaxial 3C-SiC films. *Applied physics letters* **2013,** *102* (1), 011908.

[43]   B. Gupta; M. Notarianni; N. Mishra; M. Shafiei; F. Iacopi; N. Motta, Evolution of epitaxial graphene layers on 3C SiC/Si (111) as a function of annealing temperature in UHV. *Carbon* **2014,** *68*, 563-572.

[44]   M. P. Araújo; O. Soares; A. Fernandes; M. Pereira; C. Freire, Tuning the surface chemistry of graphene flakes: new strategies for selective oxidation. *RSC Advances* **2017,** *7* (23), 14290-14301.

[45]   S. A. You; O. S. Kwon; J. Jang, A facile synthesis of uniform Ag nanoparticle decorated CVD-grown graphene via surface engineering. *Journal of Materials Chemistry* **2012,** *22* (34), 17805-17812.

[46]   K. S. Kim; Y. M. Um; J.-r. Jang; W.-S. Choe; P. J. Yoo, Highly sensitive reduced graphene oxide impedance sensor harnessing π-stacking interaction mediated direct deposition of protein probes. *ACS Applied Materials & Interfaces* **2013,** *5* (9), 3591-3598.

[47]   A. Joshi; A. Bajaj; R. Singh; P. Alegaonkar; K. Balasubramanian; S. Datar, Graphene nanoribbon–PVA composite as EMI shielding material in the X band. *Nanotechnology* **2013,** *24* (45), 455705.

[48]   Z. Li; R. J. Young; I. A. Kinloch, Interfacial stress transfer in graphene oxide nanocomposites. *ACS Applied Materials & Interfaces* **2013,** *5* (2), 456-463.

[49]   N. Mishra; M. Bosi; F. Rossi; G. Salviati; J. Boeckl; F. Iacopi, Growth of graphitic carbon layers around silicon carbide nanowires. *Journal of Applied Physics* **2019,** *126* (6), 065304.

[50]   K. Haubner; J. Murawski; P. Olk; L. M. Eng; C. Ziegler; B. Adolphi; E. Jaehne, The route to functional graphene oxide. *ChemPhysChem* **2010,** *11* (10), 2131-2139.

[51]   Q. Pan; N. Tong; N. He; Y. Liu; E. Shim; B. Pourdeyhimi; W. Gao, Electrospun mat of poly (vinyl alcohol)/graphene oxide for superior electrolyte performance. *ACS Applied Materials & Interfaces* **2018,** *10* (9), 7927-7934.

[52]   S. Sarkar; K. Raul; S. Pradhan; S. Basu; A. Nayak, Magnetic properties of graphite oxide and reduced graphene oxide. *Physica E: Low-dimensional Systems and Nanostructures* **2014,** *64,* 78-82.

[53]   N. Ghaderi; M. Peressi, First-principle study of hydroxyl functional groups on pristine, defected graphene, and graphene epoxide. *The Journal of Physical Chemistry C* **2010,** *114* (49), 21625-21630.

[54]   S. Tang; S. Zhang, Adsorption of epoxy and hydroxyl groups on zigzag graphene nanoribbons: Insights from density functional calculations. *Chemical Physics* **2012,** *392* (1), 33-45.

[55]   H. C. Schniepp; J.-L. Li; M. J. McAllister; H. Sai; M. Herrera-Alonso; D. H. Adamson; R. K. Prud'homme; R. Car; D. A. Saville; I. A. Aksay, Functionalized single graphene sheets derived from splitting graphite oxide. *The Journal of Physical Chemistry B* **2006,** *110* (17), 8535-8539.

[56]   B. Gupta; I. Di Bernardo; P. Mondelli; A. Della Pia; M. G. Betti; F. Iacopi; C. Mariani; N. Motta, Effect of substrate polishing on the growth of graphene on 3C–SiC (111)/Si (111) by high temperature annealing. *Nanotechnology* **2016,** *27* (18), 185601.

[57]   S. Oswald; W. Brückner, XPS depth profile analysis of non‐stoichiometric NiO films. *Surface and Interface Analysis: An International Journal devoted to the development and application of techniques for the analysis of surfaces, interfaces and thin films* **2004,** *36* (1), 17-22.

[58]   M. J. Kenney; M. Gong; Y. Li; J. Z. Wu; J. Feng; M. Lanza; H. Dai, High-performance silicon photoanodes passivated with ultrathin nickel films for water oxidation. *Science* **2013,** *342* (6160), 836-840.

[59]   S. Roldán; D. Barreda; M. Granda; R. Menéndez; R. Santamaría; C. Blanco, An approach to classification and capacitance expressions in electrochemical capacitors technology. *Physical Chemistry Chemical Physics* **2015,** *17* (2), 1084-1092.